

Maurizio Spurio

Particles and Astrophysics

Extra material

June 2014

Springer

Contents

List of Acronyms	1
List of experiments quoted in the book	3
Extra 1: Matter content of the Universe	11
Extra 2: The astronomical coordinate system	13
Extra 3: The Feynman Scaling and phenomenology of strong interactions	15
3.1: The Feynman Scaling	15
3.2: Hadronic interactions in Monte Carlo codes	16
3.3: Typical problems in Monte Carlo generators	18
Extra 4: The Eddington luminosity limit	19
Extra 5: Muon energy losses	21
Extra 6: Neutrino Oscillations in Matter	23
Extra 7: Experimental limits on Grand Unification Theories	27
7.1: Proton Decay	27
7.2: Magnetic Monopoles	29
References	31
References	31

List of Acronyms

AGN [Active Galactic Nuclei]
CERN [European Laboratory for Particle Physics]
CMB [Cosmic Microwave Background]
CC [Charged Current]
CR [Cosmic Ray]
DM [Dark Matter]
EAS [Extensive Air Shower]
EBL [Extragalactic Background Light]
ESA [European Space Agency]
EM [ElectroMagnetic]
ES [Elastic Scattering]
FNAL [Fermi NAtional Laboratory]
GUTs [Grand Unification Theories]
GPS [Global Positioning System]
GRBs [Gamma Ray Bursts]
GZK [Greisen Zatsepin Kuzmin]
HE [High Energy]
IACT [Imaging Air Cherenkov Technique]
IC [inverse Compton]
INFN [Istituto Nazionale di Fisica Nucleare]
ISM [InterStellar Matter]
ISS [International Space Station]
LNGS [Gran Sasso Laboratory]
LSP [Lightest Supersymmetric Particle]
MACHO [MAssive Compact Halo Object]
MSSM [Minimal Standard Supersymmetric Model]
MC [Monte Carlo]
NASA [National Aeronautics and Space Administration]
NC [Neutral Current]
NS [Neutron Star]
PMT [Photo Multiplier Tube]

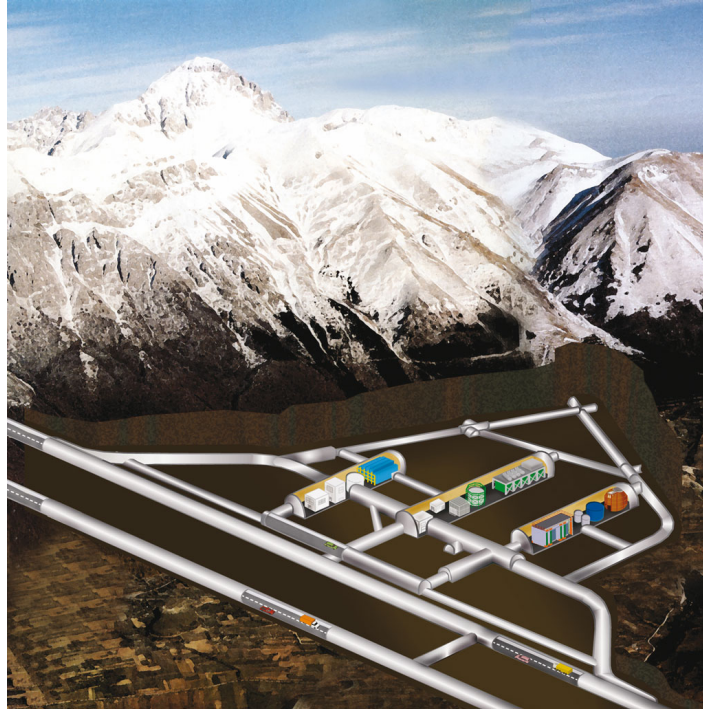


Fig. 0.1 Pictorial view of the kilometer-long tunnel system of the Gran Sasso underground laboratory, with the sketch of the three experimental halls (Photo and drawing: LNGS).

PWNe [Pulsar Wind Nebulae]
PSF [Point Spread Function]
RICH [Ring-Imaging Cherenkov detector]
SED [Spectral Energy Distribution]
SLAC [Stanford Linear Accelerator Center]
SM [Standard Model]
SNR [SuperNova Remnant]
SSC [Self-Synchrotron Compton]
SSM [Standard Solar Model]
STP [Standard Temperature and Pressure]
SUSY [Super SYmmetry]
TRD [Transition Radiation Detector]
ToF [Time of Flight]
UTC [Coordinated Universal Time]
UHECR [Ultra High Energy Cosmic Ray]
WIMP [Weakly Interacting Massive Particle]

List of experiments quoted in the book

- **ACE** [Advanced Composition Explorer].
Space mission mainly for solar particles; launched in August 1997. The spacecraft has enough propellant on board to maintain an orbit at L1 libration point until ~ 2024 .
- **AGASA** [Akeno Giant Air Shower Array].
Large area array which operated at the Akeno Observatory (100 km west of Tokyo) between 1990 and 2004.
- **AGILE** [Astro-rivelatore Gamma a Immagini Leggero].
Italian satellite for X-ray/gamma ray; launched in April, 2007.
- **AIROBICC** [AIRshower Observation By angle Integrating Cherenkov Counters].
Non-imaging counters in the HEGRA array.
- **AMS** [Alpha Magnetic Spectrometer].
The AMS-02 detector has been installed on the International Space Station on May 19, 2011. A test for AMS-02 which flies for 10 days during 1998. See: <http://www.ams02.org/>
- **ANTARES** [Astronomy Neutrino Telescope and Abyss environmental RESearch].
Neutrino telescope in the Mediterranean sea running in its complete configuration since May 2008.
- **AMANDA** [Antarctic Muon And Neutrino Detector Array].
A detector for high-energy neutrino located beneath the Amundsen-Scott South Pole Station. In 2005, after nine years of operation, it became part of its successor project, IceCube.
- **ARGO** [Astrophysical Radiation with Ground-based Observatory].
It was a cosmic ray telescope optimized for the detection of small size air showers located in Tibet and operational since 2012.
- **ATIC** [Advanced Thin Ionization Calorimeter].
Balloon-borne instrument, which has completed three successful flights over Antarctica.
- **AS γ** [Tibet Air Shower Experiment].
Scintillation counter array.

- **BAIKAL** [Baikal Deep Underwater Neutrino Telescope].
Detector in operation since 1993 for neutrino astronomy.
- **Baksan** [Baksan Neutrino Observatory].
Scientific laboratory located in the Baksan gorge (Caucasus mountains, Russia).
- **BATSE** [Burst and Transient Source Experiment].
Instrument on board the CGRO
- **BeppoSAX** [Satellite Astronomia X].
Gamma ray burst and X-ray afterglow. Operational May 1996 - April 2002.
“Beppo” stands for Giuseppe Occhialini.
- **BESS** [Balloon Experiment with a superconducting Solenoid Spectrometer].
Joint Japanese and American project for a series of experiments on balloon.
- **BLANCA** [Broad Lateral Non-imaging Cherenkov Array].
Cherenkov counter array at CASA
- **BOOMERanG** [Balloon Observations Of Millimetric Extragalactic Radiation ANd Geophysics].
Balloon-borne experiment for the CMB measurement.
- **Borexino**

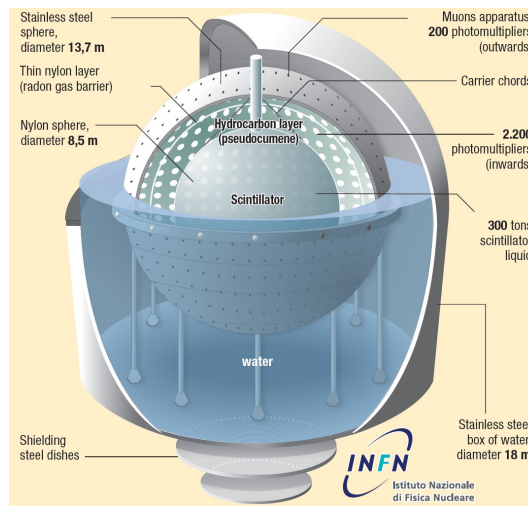


Fig. 0.2 Sketch of the Borexino detector. The scintillator is contained in a thin nylon vessel and shielded by two oil buffers separated by a second nylon vessel. The scintillator and buffers are contained within a 13.7 m stainless-steel sphere that is housed in a 16.9 m domed water tank for additional shielding against cosmic rays, external γ -rays and neutrons. Credit: INFN

Liquid scintillator detector at Gran Sasso for boron solar neutrinos.

- **CALET** [CAlorimetric Electron Telescope].
Planned experiment on the International Space Station.
- **CANGAROO** [Collaboration of Australia and Nippon for a GAMMA Ray Observatory in the Outback].

- IACT at Woomera, Australia.
- **CASA** [Chicago Air Shower Array].
Array located on Dugway Proving Grounds, Utah, USA. Operational from 1990-1998
- **CDMS** [Cryogenic Dark Matter Search].
A series of experiments to directly detect WIMPs at the Soudan Mine in northern Minnesota (USA)
- **CAPRICE** [Cosmic AntiParticle Ring Imaging Cherenkov Experiment].
Balloon-borne experiment.
- **Chandra** [NASA's Advanced X-ray Astrophysics Facility].
It was launched and deployed by Space Shuttle Columbia on July 23, 1999.
- **CHORUS** [CERN Hybrid Oscillation Research apparatus].
Neutrino experiment at CERN closed in 1997 after four years of operations.
- **CGRO** [Compton Gamma-Ray Observatory].
Space observatory with four different instruments launched using the Space Shuttle Atlantis on 1991 April 5 and operated successfully until it was de-orbited on 2000 June 4.
- **COBE** [Cosmic Background Explorer].
It was a satellite dedicated to cosmology launched in 1989 with three different instruments on board (FIRAS, DIRBE, DMR).
- **CoGeNT** [Coherent Germanium Neutrino Technology].
Dark Matter experiment at the Soudan Laboratory (USA)
- **COMPTEL** [Compton Telescope].
Imaging telescope on the CGRO for 0.8 MeV - 30 MeV γ -rays.
- **COS-B**
It was the first ESA mission, launched in 1975, to study γ -ray sources.
- **CREAM** [Cosmic Ray Energetics and Mass Balloon Experiment].
Series of ultra-long duration balloon flights for CR studies.
- **CRIS** [Cosmic Ray Isotope Spectrometer].
Experiment on board the ACE spacecraft.
- **CRESST** [Cryogenic Rare Event Search with Superconducting Thermometers].
Direct WIMPs detection experiment at LNGS
- **CRN** [Cosmic Ray Nuclei].
It flew onboard the Space Shuttle Challenger in 1985 for 9 days as a part of the NASA Spacelab program.
- **DAMA** [Dark Matter].
Series of experiment at Gran Sasso Lab for dark matter searches.
- **DICE** [Dual Imaging Cherenkov Experiment].
Cherenkov telescopes located near the CASA array.
- **DUMAND** [Deep Underwater Muon and Neutrino Detection].
Project from 1976 to 1995 for the construction of a neutrino telescope.
- **EAS-TOP** [Extensive Air Shower on Top].
Located at the top of LNGS, operational from 1991 since 2001.

- **EDELWEISS** [Expérience pour DEtecter Les Wimps En Site Souterrain].
Bolometric detectors at the underground laboratory of Modane for direct detection of dark matter.
- **EGRET** [Energetic Gamma Ray Experiment Telescope].
Experiment on the CGRO
- **Exosat** [European X-ray Observatory Satellite of ESA]
- **Fermi** [Gamma-ray Space Telescope].
Launched on June 11, 2008. It carries the LAT (formerly called the Gamma-ray Large Area Space Telescope, GLAST) and the GBM detectors.
- **Frejus** Early tracking iron calorimeter for proton decay and neutrino study.
- **GALLEX** [GALLium EXperiment].
It was a radiochemical neutrino detection experiment that ran between 1991 and 1997 at the INFN Laboratori Nazionali del Gran Sasso, Italy.
- **GAMMA** Air shower array and muon counters at Mount Aragats, Armenia.
- **GAMMA-400** [Gamma Astronomical Multifunctional Modular Apparatus].
Planned Russian satellite experiment.
- **GNO** [Gallium Neutrino Observatory].
The experiment is the successor project of GALLEX.
- **GBM** [Gamma-ray Burst Monitor].
Instrument on board the Fermi satellite.
- **HAWC** [High-Altitude Water Cherenkov Observatory].
It is a facility designed to observe TeV γ -rays and CRs currently (2014) under construction on the Sierra Negra volcano near Puebla, Mexico.
- **HEAO-3** [High Energy Astrophysics Observatory].
The satellite operated between 1979 and 1981 and it carried three high-energy-astrophysics instruments.
- **HEAT** [High Energy Antimatter Telescope].
Balloon-borne experiment.
- **HERD** [High Energy Cosmic Radiation Detection].
Planned program onboard China's Space Station.
- **HEGRA** [High Energy Gamma Ray Astronomy].
Cherenkov Telescopes on Canary Islands, operational from 1998 until 2002.
- **HESS** [High Energy Stereoscopic System].
System of five IAC telescopes in Namibia. Fully operational since December 2003.
- **HiRes** [High Resolution Fly's Eye detector].
Fluorescence observatory for CRs that operated in the Utah desert from May 1997 until April 2006.
- **Homestake** [Mine Solar neutrino experiment].
It was a deep underground gold mine located in South Dakota (USA) where the solar neutrino problem was first raised by Raymond Davis Jr.
- **Haverah Park**. Air shower array of Leeds University, operational until 1993.
- **Hubble** [Hubble space telescope].
It is a space telescope that was carried into orbit by a Space Shuttle in 1990.

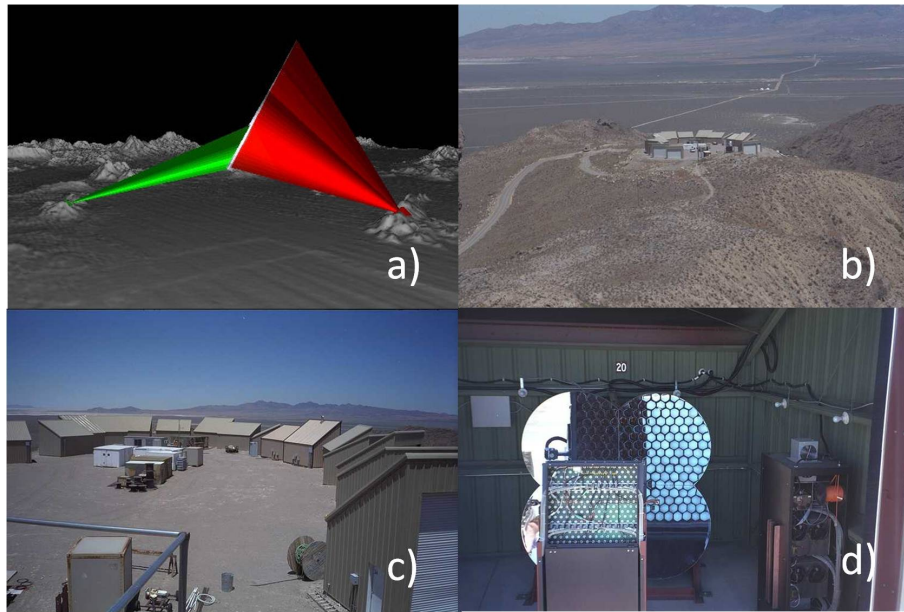


Fig. 0.3 (a) The Hires detector was an observatory monitoring on every clear, moonless night the atmosphere over a 3000 square kilometer ground area from two sites. Each site (b,c) has an array of large mirrors equipped with fast photomultiplier cameras, which is visible in (d). Courtesy HiRes collaboration. <http://www.physics.adelaide.edu.au/astrophysics/hires/>

- **Kamiokande** [Kamioka Nucleon Decay Experiment].
One of the first nucleon decay experiment used also for neutrino astrophysics.
- **KamLAND** [Kamiokande Liquid scintillator ANTineutrino Detector].
Liquid scintillator detector in the old location of Kamiokande.
- **KASCADE** [KARlsruhe Shower Core and Array Detector].
Operational since 1996 and later extended as KASCADE-Grande.
- **KGF** [Kolar Gold Field].
One of the first nucleon decay experiment in India.
- **K2K** [KEK to Kamioka].
Long baseline neutrino experiment that ran from June 1999 to November 2004 in Japan.
- **IceCube** [Ice Cube neutrino observatory].
Neutrino detector at the Amundsen-Scott South Pole Station in Antarctica.
- **IMB** [Irvine Michigan Brookhaven experiment]
- **IMP** [Interplanetary Monitoring Platform].
The IMP were part of the Explorer program, which was a NASA space exploration program that provides flight opportunities for physics, heliophysics, and astrophysics investigations from space.
- **IMAX** [Isotope Matter Antimatter Experiment].

It is a balloon-borne, superconducting magnet spectrometer experiment which successful flight in 1992.

- **INTEGRAL** [INTErnational Gamma-Ray Astrophysics].
It was launched by the ESA into Earth orbit in 2002.
- **ISEE-3** [International Sun/Earth Explorer 3].
Spacecraft also known as International Cometary Explorer (ICE). It was launched August 12, 1978 as part of a NASA and ESA program to study the interaction between the Earth's magnetic field and the solar wind.
- **ISOMAX** [Isotope Magnet Experiment].
- **JACEE** [Japanese-American Collaborative Emulsion Experiment].
Balloon-borne experiment mainly for cosmic-ray.
- **LAT** [Large Area Telescope].
Experiment for γ -ray detection on the Fermi satellite.
- **LEP** [Large Electron Positron collider].
Collider in operation at CERN before the advent of LHC.
- **LHC** [Large Hadron Collider].
- **LHAASO** [Large High Altitude Air Shower Observatory].
Proposed experiment for very high energy γ -ray source survey.
- **LSD** [Liquid Scintillation Detector].
Old experiment for supernova neutrinos under the Mount Blanc.
- **LVD** [Large Volume Detector].
Apparatus for supernova neutrinos detection at LNGS.
- **MACRO** [Monopololes And Cosmic Ray Observatory].
Large underground apparatus at the LNGS, running from 1994 to 2001.
- **MAGIC** [Major Atmospheric Gamma-ray Imaging Cherenkov].
A system of two Imaging Cherenkov telescopes on La Palma, Canary Islands. The first telescope is operational since 2003.
- **MASS** [Matter Antimatter Superconducting Spectrometer].
Balloon-borne experiment which flown in different configurations.
- **MAXIMA** [Millimeter Anisotropy eXperiment IMaging Array].
Balloon-borne experiment for the CMB measurement.
- **Milagro**. Water Cherenkov experiment near Los Alamos. It stopped taking data in April 2008 after seven years of operation.
- **MIA** [Muon Array].
Muon detectors associated with the CASA array.
- **MINOS** [Main Injector Neutrino Oscillation Search].
It was a long-baseline neutrino oscillation experiment in USA which run from 2006 to 2012.
- **NOMAD** [Neutrino Oscillation MAGnetic Detector].
It was a short base-line experiment for $\nu_\mu \rightarrow \nu_\tau$ oscillations in the CERN neutrino beam.
- **NUSEX** [NUcleon Stability EXperiment].
Under the Mount Blanc laboratory (Italy). One of the first nucleon decay experiment.

- **OPERA** [Oscillation Project with Emulsion-tRacking Apparatus].
It was a long base-line experiment for $\nu_\mu \rightarrow \nu_\tau$ oscillations from CERN to LNGS.
- **OSO-3** [Third Orbiting Solar Observatory].
- **OSSE** [Oriented Scintillation Spectrometer].
One of the four experiment in board the CGRO for γ -rays in the 0.05-10 MeV energy range.
- **PAMELA** [Payload for Antimatter Matter Exploration and Light-nuclei Astrophysics].
A cosmic ray research module attached to an Earth orbiting satellite launched on 15 June 2006.
- **PAO** [Pierre Auger Observatory].
The largest running EAS located in Argentina.
- **Planck**. ESA mission to observe the first light in the Universe. It was launched on 14 May 2009 and turned off on 23 October 2013.
- **PPB-BETS** [Polar Patrol Balloon (PPB)- Balloon-borne Electron Telescope with Scintillating fibers (BETS)].
A long duration balloon experiment in Antarctica, lasted 13 days in 2004.
- **ROSAT** [High-resolution X-ray satellite].
It was launched June 1, 1990 and ended on February 12, 1999.
- **RUNJOB** [RUssian-Nippon JOint Balloon Experiment].
Balloon-borne experiment.
- **RXTE** [Rossi X-ray Timing Explorer Laboratory].
- **SAGE** [Soviet-American Gallium Experiment].
It was a Russian-American experiment to measure the solar neutrino flux.
- **SAS-2** [The Small Astronomy Satellite-NASA]
- **SK** [Super-Kamiokande].
Evolution of the Kamiokande experiment, starting data taking in 1996.
- **SNO** [Sudbury Neutrino Observatory].
- **Soudan**. Experiment in a mine for the nucleon stability.
- **SUGAR** [Sydney University Giant Air shower Recorder].
It was operational in Australia from 1968 to 1979.
- **Swift** [Gamma-Ray Burst Mission].
Launched November 20, 2004.
- **T2K** [Tokai to Kamioka].
It is a long baseline experiment in Japan in operation since 2009.
- **TA** [Telescope Array].
Extensive air shower observatory.
- **TIGER** [Trans-Iron Galactic Element Recorder].
Balloon-borne experiment.
- **TRACER** [Transition Radiation Array for Cosmic Energetic Radiation].
Balloon-borne experiment.
- **Tunka** [Tunka array].
A non-imaging Cherenkov array situated in Siberia close to lake Baikal.

- **Ulysses.** Launched in 1990 and decommissioned in 2009. It was a robotic space probe that designed to study the Sun as a joint venture of NASA and ESA.
- **Vela.** It was the name of a group of satellites developed by the United States to monitor compliance with the 1963 Partial Test Ban Treaty by the Soviet Union, and other nuclear-capable states.
- **VERITAS** [Very Energetic Radiation Imaging Telescope Array System].
IACT operating in Arizona (USA).
- **Voyager.** The Voyager program was an American scientific program that launched in 1977 two unmanned space missions (Voyager 1 and Voyager 2) to study the outer solar system.
- **Whipple** [Gamma-Ray Telescope on Mt. Hopkins, Arizona].
The pioneering IACT experiment, predecessor and operating in the same site of VERITAS in Arizona.
- **WMAP** [Wilkinson Microwave Anisotropy Probe].
It is a spacecraft launched on 2001 which measures differences in the temperature of the Big Bang's remnant radiant across the full sky.
- **XMM-Newton** [X-ray Multi-Mirror Mission].
- **XMASS.** Series of liquid Xenon experiment for DM searches in Japan.
- **Yakutsk** [EAS array at Yakutsk].
Array operating since 1967 by the Institute of Cosmophysical Research and Aeronomy, Siberia

Extra 1: Matter content of the Universe

In June 2001, NASA launched a space mission dedicated to cosmological measurements, the WMAP satellite. The first results from this mission were presented in 2003, showing small anisotropies in the CMB radiation. The WMAP's measurements played a key role in establishing the current Standard Model of Cosmology, §13.1. According to the anisotropies map, subtle fluctuations in temperature were imprinted on the CMB when the cosmos was about 370,000 years old. Apparently, these “ripples” gave rise to the present vast cosmic network of galaxy clusters and dark matter.

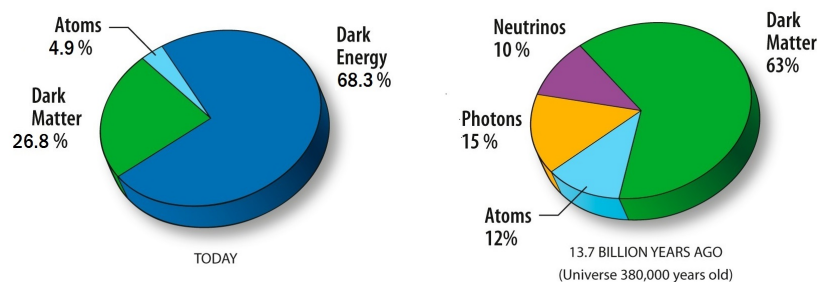


Fig. 0.4 (Left side: Today) The data collected by WMAP [E-05] and Planck [E-10] experiments reveals that the matter content of the Universe include $\sim 5\%$ atoms (“ordinary” matter). Dark matter comprises $\sim 27\%$ of the Universe. This matter, different from atoms, does not emit or absorb light, it is “dark”. It has only been detected indirectly by its gravity. $\sim 68\%$ of the Universe is composed of “dark energy”, that acts as a sort of repulsive gravity. This dark energy is responsible for the present-day acceleration of the universal expansion. The data are accurate to two digits, so the total of these numbers is not 100%. As the size of the Universe increases with time, the relative contribution of dark energy and other form of energy changes from the decoupling era (Right side: Universe age of 380000 years) and the present era. Adapted from NASA/WMAP Science Team (ESA/Hubble)

A second space mission, Planck, was launched by the European Space Agency (ESA) in collaboration with NASA in May 2009. It has been measuring the CMB anisotropies at a higher resolution than WMAP.

Planck was designed to observe anisotropies of the CMB at microwave and infra-red frequencies, with high sensitivity and small angular resolution. Planck was launched in May 2009, reaching the Earth/Sun second Lagrangian point by July, and by February 2010 had successfully started a second all-sky survey. On 21 March 2013, the mission's all-sky map of the CMB was released. The spacecraft carries two instruments: the Low Frequency Instrument (LFI) and the High Frequency Instrument (HFI). The instruments can detect both the total intensity and polarization of photons, and together cover though 9 different bands a frequency range from 30 to 857 GHz. The CMB spectrum peaks at a frequency of 160.2 GHz. Planck's passive and active cooling systems allowed its instruments for the first \sim three years to maintain a temperature of -273.05°C .

When the temperature of the Universe was $\sim 3000\text{ K}$, electrons and protons combined to form neutral hydrogen (the so-called *recombination* process). The energy contents of the Universe immediately before recombination epoch (§13.1) was under the form of a tightly coupled photon-lepton-baryon fluid that can be studied using basic fluid mechanics equations. A perfect homogenous fluid has the same temperature T . The precise observation of the CMB radiation at different directions in the sky provide a map which allows to determine temperature anisotropies.

These temperatures anisotropies can be expressed in terms of spherical harmonics functions $Y_{\ell m}(\theta, \phi)$:

$$\frac{\delta T}{T}(\theta, \phi) = \sum_{\ell=2}^{+\infty} \sum_{m=-\ell}^{+\ell} a_{\ell m} Y_{\ell m}(\theta, \phi) \quad (0.1)$$

through appropriate values of the $a_{\ell m}$ coefficients. If the temperature fluctuations are assumed to be Gaussian, as appears to be the case, all of the information contained in CMB maps can be compressed into the power spectrum, essentially giving the behavior of the parameters $C_\ell \equiv \langle |a_{\ell m}|^2 \rangle$ as a function of ℓ . The salient characteristics of the anisotropy spectrum (the existence of peaks and troughs; the spacing between adjacent peaks; and the location of the first peak) depend in decreasing order of importance on the initial conditions, the energy contents of the Universe before recombination and those after recombination.

The WMAP and Planck data are very well fit by a Universe whose content presently consists of a small fraction ($\sim 5\%$) of ordinary baryonic matter; $\sim 25\%$ of “cold” dark matter that neither emits nor absorbs light (see Chapter 13). The content is dominated ($\sim 70\%$) by some unknown form of *dark energy* that accelerates the expansion of the Universe. Together with other cosmological data, the results from these experiments suggest a flat geometry for the Universe. According to the latest Planck results, the Hubble constant is $67.80 \pm 0.77 \text{ km s}^{-1} \text{ Mpc}^{-1}$, indicating that the Universe is $\tau_{H_0} = (13.798 \pm 0.037) \times 10^9$ years old (the Hubble time), and contains 4.9% of ordinary matter, 26.8% of dark matter and 68.3% of dark energy, see Fig. 0.4.

Extra 2: The astronomical coordinate system

The position of galactic objects on the sky can be defined using the **galactic coordinate system**. This is a spherical coordinate system, having the Sun at the origin, where each object is identified by a *galactic latitude*, b , and a *galactic longitude*, ℓ , measured in degrees. The galactic latitude measures the angular distance of an object with respect to the galactic plane, Fig. 0.5. The galactic longitude measures the angular distance of an object eastward along the galactic equator from the galactic center, Fig. 0.6. The galactic coordinate system is used in many plots of the book (Figures 8.3, 8.6, 9.7, 10.17)

The **equatorial coordinate system** is another widely used celestial coordinate system. It is usually implemented in spherical coordinates, where the two angular variables are the declination and the right ascension. The origin of the system is the center of the Earth, and a fundamental plane consisting of the projection of the Earth's equator onto the celestial sphere defines the celestial equator. The declination, δ , measures the angular distance of an object perpendicular to the celestial equator, positive to the north, negative to the south. The right ascension, α or RA, measures the angular distance of an object eastward along the celestial equator from a well-defined point, called the vernal equinox. Analogous to the terrestrial longitude, the RA is usually measured in sidereal hours, minutes and seconds instead of degrees, a result of the method of measuring right ascensions by timing the passage of objects across the meridian as the Earth rotates. In this system, the galactic centre is at $\text{RA}=17^{\text{h}}45^{\text{m}}$ and $\delta = -29^{\circ}00'$.

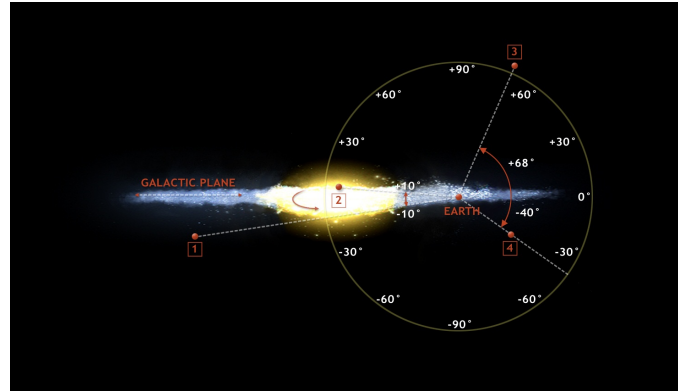


Fig. 0.5 The galactic coordinates use the Sun as the origin. The galactic latitude (b) measures the angle of the object above the galactic plane. The galactic plane is like the Earth's Equator, and like the Equator, it is at 0° latitude. The Earth is on the galactic plane. Four objects are indicated, which have different latitudes. From Chandra X-ray observatory (credit: NASA)

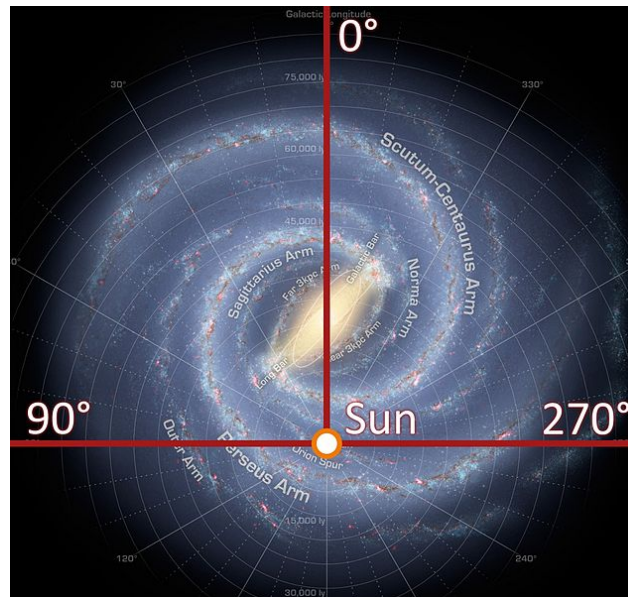


Fig. 0.6 The galactic longitude (ℓ) is measured with primary direction from the Sun to the center of the Galaxy in the galactic plane. Galactic coordinates go from 0° (the direction of the galactic center) to 360° . This figure uses adapted infrared images from NASA's Spitzer Space Telescope. The elegant spiral structure is dominated by just two arms wrapping off the ends of a central bar of stars. (Credit: NASA)

Extra 3: The Feynman Scaling and phenomenology of strong interactions

3.1 The Feynman Scaling

The hadron cross-sections depend on the energy of the incoming particle. In general this quantity depends on the choice of the system reference frame. A Lorentz invariant inclusive cross-section¹ for the production of secondary particles in a high energy hadronic interaction is given by the expression:

$$f(ab \rightarrow cX) = E_c \frac{d^3\sigma}{dp_c^3} = \frac{E_c}{p_c^2} \frac{d^3\sigma}{dp d\Omega} \quad (0.2)$$

a, b are the initial colliding particles, C is the produced particle of interest and X represents all other particles produced in the collision. $d^3\sigma/dp_c^3$ is the differential cross-section for detecting the particle c within the momentum phase-space dp_c^3 . E_c is the total energy of the observed particle C and $d\Omega$ the differential solid angle. It is found that the Lorentz invariant inclusive cross-section can be written as a function of three variables (we omit the subscript c):

$$E \frac{d^3\sigma}{dp^3} = f(s; x^*; p_t) \quad (0.3)$$

where s is the center-of-mass energy squared, p_t the component of the momentum perpendicular to the incoming particles and x^* is the fraction of maximum available longitudinal momentum (p_l) in the center-of-mass frame (variable denoted by a $*$). The x variable is defined as:

$$x \equiv \frac{p_l^*}{p_{l_{max}}} \quad (0.4)$$

¹ A *exclusive* measurement implies that energy and momenta of all the products have been measured. *Inclusive* measurement means that some of the products may have been left unmeasured. Exclusive measurements are dedicated to one, well defined physics process, while inclusive measurements may tell about a collection of processes. For instance, the inclusive pion production in proton-proton collision can be represented as $pp \rightarrow \pi + X$, where X is the unobserved status.

and it is called the Feynman variable. The Feynman hypothesis which is the foundation of the Feynman scaling model states that at very high energies (when $s \gg m_p$, where m_p is the proton mass), the invariant cross-section can be expressed in terms of only two variables:

$$\lim_{s \rightarrow \infty} f(s; x^*; p_t) = f(x^*; p_t) \quad (0.5)$$

The variables x and p_t becomes asymptotically independent of the energy, E .

Using the formalism just introduced, the Feynman- x is limited to $-1 < x < 1$. The condition that x remains fixed as $s \rightarrow \infty$ ensures that the particle produced is a fragment of the beam particle or of the target particle (depending on the sign of p_t^*). These are called respectively the beam and the target fragmentation regions. For $p_t^* > 0$ (forward fragmentation region) there is no dependence on the target in the scaling limit. The distribution is similarly independent of the nature of the projectile when $p_t^* < 0$. The kinetic region $x \sim 0$ as $s \rightarrow \infty$ is called the *central region*: in this region the Feynman scaling is violated.

The invariance with energy of the inclusive distributions, i.e. scaling, in the fragmentation region is the hypothesis of the so-called *limiting fragmentation*. Regarding CR showers, the particles in the narrow angle forward cone are particularly important as they are the principal carriers of the energy and determine to a good extent the longitudinal development of air showers. Of particular importance is the projectile fragmentation because it affects the development of a shower. The target fragments are in this context of lesser importance. Thus, the secondary production is independent of the target nature. The number of charged particles produced, i.e., the charge multiplicity, increases logarithmically with the center-of-mass energy. As a consequence of the Feynman scaling, the ratio between the energy carried by the secondary and that of the colliding proton is almost constant.

3.2 Hadronic interactions in Monte Carlo codes

High-energy hadronic interactions are dominated by the inelastic cross-section, characterized by the production of a large number of particles. Most of the interactions produce a large number of particles with small transverse momentum with respect to the collision axis (the so-called *soft* production). Only a small fraction of events results in central collisions between elementary constituents and produce particles at large transverse momentum (*hard* production). QCD is able to compute the properties of hard interactions. Here the momentum transfer between the constituents is large enough (and the strong running coupling constant is small enough) to apply the ordinary perturbative theory. As the soft multiparticle production is characterized by small momentum transfer, we are forced to build models and adopt alternative non-perturbative approaches.

The lack of a detailed theoretical description of soft hadronic interactions is coupled with the lack of experimental data for these processes from experiments at accelerators or colliders. The modeling of high energy hadronic interactions for CR

studies has to deal with the fact that part of the center-of-mass energy for hadron-hadron collisions extends above the actual possibilities of collider machines. Most recent experimental data extends up to $\sqrt{s} = 7$ TeV at the LHC. Thus one is forced to extrapolate these measurements into regions not yet covered by collider data. In addition at colliders the particles hard scattered in the collisions are the best studied. In the fragmentation regions (target or projectile), the particles produced at small angles escape into the beam pipe and hence they are not observed. For the development of a CR shower, particles produced in the fragmentation region are the most important since they are the ones that carry the energy down the atmosphere and produce the bulk of secondary particles in the cascade. Finally, part of CR collisions in atmosphere are nucleus-nucleus collisions. In this case, the data from fixed target experiments extends only up to few GeV/nucleus in the laboratory frame. These are the reasons why interaction models constitute a major contribution to systematic uncertainties in CR physics.

A Monte Carlo simulation treating the cascade development, the so-called shower propagation code, can implement different hadronic interaction models, referred as *event generators*. One of the most used shower propagation code is CORSIKA, §4.5, a general-purpose Monte Carlo code created by the KASCADE group. The event generators are sub-packages that can be easily inserted in an existing shower simulation program. Several models have been developed into generators that incorporate partonic ideas and QCD concepts (as the quark confinement inside the hadrons) into an homogenous scheme to include hard and soft components into the same framework. The software interface allows the implementation without altering the general structure of the shower propagation code. The use of a single air shower code with different hadronic interaction models allows mutual comparison between the models. Below, some of the most used generators are shortly described.

VENUS, QGSJET, and DPMJET are based on a phenomenological theory (called *Gribov-Regge theory - GRT*), which describes the elastic scattering and, via the optical theorem, the total hadronic cross-section as a function of energy.

In a description of the diffraction pattern of the incident particle wave on a target, similar to that of classical optics, the total cross-section $\sigma_{tot} = \sigma_{el} + \sigma_{inel}$, is related to the elastic differential cross-section at $t = -Q^2 \rightarrow 0$ through the so-called *optical theorem*. Within QCD the growth of σ_{tot} with energy as $\sigma_{tot} \propto s^{\alpha_0}$, where s is the square of the center-of-mass energy and α_0 a positive parameter, can be associated with the increasing contribution of soft gluons exchanges. This behavior would be divergent at large s ; these divergences must be overcome with appropriate mathematical methods. In the GRT model the observed rise of the cross-sections is a consequence of the exchange of multiple virtual particles called *pomerons*. Inelastic processes are described by the production of pomerons leading to two color strings, each that fragment subsequently into color-neutral hadrons. While the exchange of virtual particles is a common feature for all implementations of the GRT, the models differ in the way the production and decay of the strings is realized.

SIBYLL is a *minijet* model. It simulates a hadronic reaction as a combination of one underlying soft collision in which two strings are generated and a number of minijet pairs leading to additional pairs of strings with higher p_t ends. In this model,

the rise of the cross-section is due to the minijet production only. HDPM is a purely phenomenological generator which uses detailed parameterizations of $p\bar{p}$ collider data for particle production. The extensions to reactions with nuclei and to energies beyond the collider energy range are somewhat arbitrary. HDPM and SIBYLL employ for nuclear projectiles the superposition model assuming that reactions for each of the projectile nucleon are independent from the presence of other nucleons. EPOS contains important improvements concerning hard interactions and nuclear and high-density effects.

3.3 Typical problems in Monte Carlo generators

A full Monte Carlo chain consists of several steps. It requires a detailed simulation of all physical processes occurring during the shower development and requires a correct treatment of energy losses and stochastic processes. Finally, a detector simulation is needed to reproduce Monte Carlo data in the same format of experimental data.

Two requirements have to be fulfilled in the exploitation of Monte Carlo codes, which are in some sense conflicting between themselves. On one hand, we need a reliable physics generator to control the data quality, to validate the analysis software, to evaluate the detector capabilities and to produce unfolding outputs (i.e., physics results which are independent of the characteristic of a specific detector). In this context, a fast simulation tool is needed. On the other hand, if it is necessary to test theoretical hypotheses and eventually infer physical parameters, a full simulation taking into account all physical phenomena is needed. A Monte Carlo generator of a shower in the atmosphere should compute the first interaction point of primary CRs on the basis of the input cross-sections, describe collisions occurring in atmosphere using different models, propagate the electromagnetic and hadronic components of the shower considering the actual mean free path of particles. In this case, the complexity of the simulation requires long computing time: the statistics is strongly limited by the slow data processing.

In some cases, parameterized generators are used as fast tools for the cross-check with experimental data. One example of a parameterized generators is reported in §11.6

Extra 4: The Eddington luminosity limit

Electromagnetic radiation can be produced from different emission mechanisms. When the energy production occurs by conversion of gravitational potential energy through accretion mechanisms, as for instance in the case of microquasars (§6.7.2), AGN (§9.9) or for some GRBs (§8.9), a limit, referred to as the *Eddington luminosity* or the *Eddington limit*, exists. The Eddington limit gives the maximum luminosity that an astrophysical object can achieve. It is not possible to generate arbitrarily large luminosities by allowing matter to fall at a sufficiently great rate onto a black hole. If the luminosity is too large, radiation pressure would blow away the infalling matter. The limiting luminosity can be determined using hydrostatic equilibrium between the inward gravity force and the outward radiation pressure force.

It is assumed that the infalling matter is fully ionized and in the form of an electron-proton plasma. The radiation pressure is provided by Thomson scattering of the radiation by electrons in the plasma. Due to the mass difference between electrons and protons, we can assume the gravity force to be due to protons and the radiation pressure to act upon electrons. Since the plasma must remain neutral, such pressure acts between protons and electrons as an electrostatic action.

The inward gravitational force on an electron-proton pair at distance r from the centre of the massive object M is

$$f_g = \frac{GM(m_p + m_e)}{r^2} \simeq \frac{GMm_p}{r^2} . \quad (0.6)$$

At the position r there is an incident flux density of photons N_γ [$\text{cm}^{-2} \text{s}^{-1}$]. The flux density of photons at a distance r from the source depends on the source luminosity L_γ [erg s^{-1}] and corresponds to:

$$N_\gamma = \frac{L_\gamma}{4\pi r^2(h\nu)} \quad (0.7)$$

If interacting, each photon imparts a momentum $p = h\nu/c$ to an electron through Thomson scattering. This process has a cross-section $\sigma_T = 0.66 \times 10^{-24} \text{ cm}^2$. Therefore, the force acting on the electron (the *radiation pressure force*) is the mo-

mentum communicated to it per second by the incident photon flux

$$f_r = \sigma_T \cdot N_\gamma \cdot p = \frac{L_\gamma \sigma_T (h\nu/c)}{4\pi r^2 (h\nu)} \quad (0.8)$$

when (0.7) is inserted. Equating the force (0.8) to the inward gravitational force (0.6), we obtain the value of the source luminosity L_γ^E that maintains the equilibrium between forces:

$$\frac{L_\gamma^E \sigma_T}{4\pi r^2 c} = \frac{GMm_p}{r^2} \quad \rightarrow \quad L_\gamma^E = \frac{4\pi GMm_p c}{\sigma_T} \quad (0.9)$$

that corresponds to the Eddington luminosity. If the luminosity of a spherically symmetric source of mass M exceeds that value, the radiation pressure will stop any further matter infall. The limiting luminosity is independent of the radius r and depends only upon the mass M of the emitting region and universal constants. Inserting the numerical values, and measuring the mass M in terms of the solar mass $M_\odot = 2.0 \times 10^{33}$ g, the expression for the Eddington luminosity can be rewritten

$$L_\gamma^E = 1.3 \times 10^{38} \left(\frac{M}{M_\odot} \right) \text{ erg/s} . \quad (0.10)$$

The spherically symmetric result provides useful constraints for models of high energy astrophysical phenomena. For a $10^9 M_\odot$ black hole, the corresponding Eddington limit is $\sim 2 \times 10^{47}$ erg/s. It is possible to exceed that limit by adopting different geometries for the source region, but not by a large factor.

Extra 5: Muon energy losses

Muon energy losses are usually divided into continuous and discrete processes. The former is due to ionization, which depends weakly on muon energy and can be considered nearly constant for relativistic particles. For muons below ~ 500 GeV, this is the dominant energy loss process. For muons reaching great depths, discrete energy losses become important: bremsstrahlung (“br”), direct electron-positron pair production (“pair”) and electromagnetic interaction with nuclei (photoproduction, “ph”). In these radiative processes energy is lost in bursts along the muon path. In general the total muon energy loss is parameterized as:

$$\frac{dE_\mu}{dX} = -\alpha - \beta E_\mu \quad (0.11)$$

where X is the thickness of crossed material in g cm^{-2} and $\beta = \beta_{\text{br}} + \beta_{\text{pair}} + \beta_{\text{ph}}$ is the sum of fractional energy losses in the three mentioned radiation processes, see Fig. 0.7. As the rock compositions are different for different underground experiments, the so-called *standard rock* is defined as a common reference. The standard rock is characterized by density $\rho = 2.65 \text{ g cm}^{-3}$, atomic mass $A = 22$ and charge $Z = 11$. The thickness X is commonly given in units of meters of water equivalent (1 m.w.e. = 10^2 g cm^{-2}).

The factors α and β in Eq. (0.11) are mildly energy dependent as well as dependent upon the chemical composition of the medium: in particular $\alpha \propto Z/A$ and $\beta \propto Z^2/A$. Typical values are $\alpha \simeq 2 \text{ MeV g}^{-1} \text{ cm}^2$ and $\beta \simeq 4 \times 10^{-6} \text{ g}^{-1} \text{ cm}^2$. The critical energy is defined as the energy at which ionization energy loss equals radiative energy losses: $\epsilon_\mu = \alpha/\beta \simeq 500 \text{ GeV}$.

The general solution of Eq. (0.11) corresponds to the average energy $\langle E_\mu \rangle$ of a beam of muons with initial energy E_μ^0 after penetrating a depth X :

$$\langle E_\mu(X) \rangle = (E_\mu^0 + \epsilon_\mu) e^{-\beta X} - \epsilon_\mu \quad (0.12)$$

The minimum energy required for a muon at the surface to reach slant depth X is the solution of Eq. (0.12) with residual energy $E_\mu(X) = 0$:

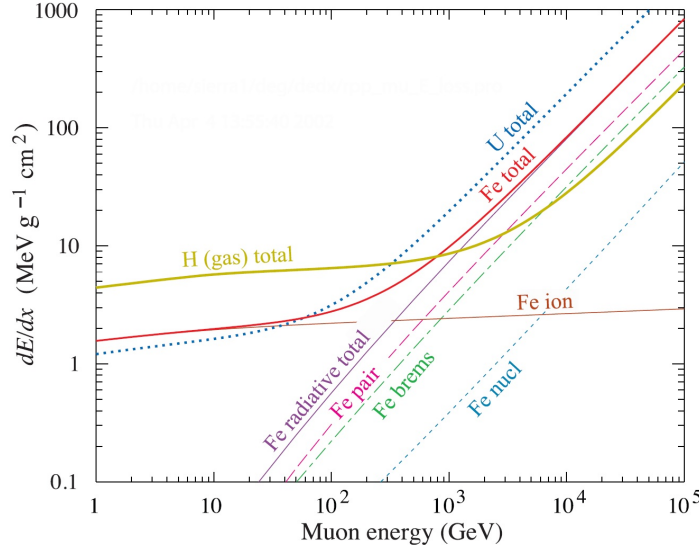


Fig. 0.7 The average energy loss of a muon in hydrogen, iron, and uranium as a function of muon energy. Contributions to dE/dx in iron from ionization (“ion”) and the processes of bremsstrahlung (“brems”), direct electron-positron pair production (“pair”) and electromagnetic interaction with nuclei (“nucl”) are also shown. Credit: The PDG [E-08]

$$E_{\mu,\min}^0 = \epsilon_{\mu}(e^{\beta X} - 1) \quad (0.13)$$

The range R for a muon of energy E_{μ}^0 , i.e. the underground depth that this muon will reach, is:

$$R(E_{\mu}^0) = \frac{1}{\beta} \ln\left(1 + \frac{E_{\mu}^0}{\epsilon_{\mu}}\right) \quad (0.14)$$

The above quantities are average values. For precise calculations of the underground muon flux one needs to take into account the fluctuations inherent in the radiative processes. Because of the stochastic character of muon interaction processes with large energy transfers (e.g. bremsstrahlung) muons are subject to a considerable range straggling. The higher E_{μ}^0 is, the more dominant are the radiation processes and the more important are the fluctuations in the energy loss which broaden the distribution of the range [E-03]. Typically, a 100 GeV (1 TeV) muon travels ~ 400 m (2500 m) in water.

Extra 6: Neutrino Oscillations in Matter

In vacuum oscillation, we can re-write the time evolution of mass eigenstates

$$|\nu_j(t)\rangle = e^{-E_j t} |\nu_j(0)\rangle \quad (0.15)$$

in the simplified 2-flavor oscillation as:

$$i \frac{d}{dt} \begin{pmatrix} \nu_1 \\ \nu_2 \end{pmatrix} = \begin{pmatrix} E_1 & 0 \\ 0 & E_2 \end{pmatrix} \begin{pmatrix} \nu_1 \\ \nu_2 \end{pmatrix} \simeq \begin{pmatrix} \frac{m_1^2}{2p} & 0 \\ 0 & \frac{m_2^2}{2p} \end{pmatrix} \begin{pmatrix} \nu_1 \\ \nu_2 \end{pmatrix} + \begin{pmatrix} p & 0 \\ 0 & p \end{pmatrix} \begin{pmatrix} \nu_1 \\ \nu_2 \end{pmatrix}. \quad (0.16)$$

After substitution of ν_1 and ν_2 with their expression in terms of, e.g., ν_e and ν_μ

$$\begin{pmatrix} \nu_e \\ \nu_\mu \end{pmatrix} = \begin{pmatrix} \cos \vartheta & \sin \vartheta \\ -\sin \vartheta & \cos \vartheta \end{pmatrix} \begin{pmatrix} \nu_1 \\ \nu_2 \end{pmatrix} \quad (0.17)$$

we have the time evolution of flavor eigenstates that satisfies the Schrödinger equation

$$i \frac{d}{dt} \begin{pmatrix} \nu_e \\ \nu_\mu \end{pmatrix} = H_0 \begin{pmatrix} \nu_e \\ \nu_\mu \end{pmatrix} \quad \text{where} \quad H_0 = \frac{\Delta m^2}{4E} \begin{pmatrix} -\cos 2\vartheta & \sin 2\vartheta \\ \sin 2\vartheta & \cos 2\vartheta \end{pmatrix} \quad (0.18)$$

is the Hamiltonian in vacuum. Note that in (0.16) the last term $p \cdot \mathcal{I}$, where $\mathcal{I} \equiv \begin{pmatrix} 1 & 0 \\ 0 & 1 \end{pmatrix}$ is a multiple of the identity matrix, can be omitted as it introduces a constant phase factor which does not affect the oscillations.

The Hamiltonian of the neutrino system in matter H_m , differs from the H_0 : $H_m = H_0 + V_{int}$, where V_{int} describes the interaction of neutrinos with matter. However, the different behavior of ν_e with respect to ν_μ and ν_τ must be taken into account. The Feynman diagrams with a Z^0 exchange (Fig. 12.4a) are the same for ν_e , ν_μ and ν_τ . The diagram with W^\pm exchange (Fig. 12.4b) exists only for the ν_e , giving an additional term for the neutrino potential. The latter results in an effective extra-potential for the ν_e flavor, $V_e = \pm \sqrt{2} G_F N_e$, where G_F is the Fermi constant

of weak interactions and N_e the electron density in the material. The positive (negative) sign applies to electron neutrinos (antineutrinos). This potential difference is proportional to the electron density N_e , and has the numerical value:

$$V_e = \sqrt{2}G_F N_e = \sqrt{2}G_F \frac{\rho}{m_p} Y_e = 3.8 \times 10^{-14} \left(\frac{\rho}{\text{g cm}^{-3}} \right) \left(\frac{Y_e}{0.5} \right) \text{ eV} \quad (0.19)$$

where m_p is the proton mass and Y_e is the number of electrons per nucleon.

This different contribution to the scattering amplitudes corresponds to a different *refraction index* of the ν_e with respect to ν_μ and ν_τ . This is called the MSW effect, from the names of the discoverers Mikheyev–Smirnov–Wolfenstein.

Therefore, the effective Hamiltonian which governs the propagation of neutrinos in matter, H_m , contains an extra element, and can be written as

$$H_m = H_0 + \begin{pmatrix} V_e & 0 \\ 0 & 0 \end{pmatrix} = H_0 + \begin{pmatrix} V_e/2 & 0 \\ 0 & -V_e/2 \end{pmatrix} = \frac{\Delta m^2}{4E} \begin{pmatrix} -\cos 2\vartheta + \xi & \sin 2\vartheta \\ \sin 2\vartheta & +\cos 2\vartheta - \xi \end{pmatrix} \quad (0.20)$$

in the first equality, we have subtracted a multiple $V_e/2 \cdot \mathcal{I}$ of the identity matrix \mathcal{I} without modifying the physics. The quantity ξ is defined, for ν_e , as:

$$\xi \equiv \frac{2\sqrt{2}G_F N_e E}{\Delta m^2} \quad (0.21)$$

the opposite sign holds for antineutrinos. The solution of the corresponding Schrödinger equation is simple in the case where the matter density is constant. If we indicate the effective mixing angle in matter as ϑ_m and the effective difference of squared masses as Δm_{eff}^2 , we can write the Hamiltonian in matter using the same form as the vacuum Hamiltonian:

$$H_m = \frac{\Delta m_{eff}^2}{4E} \begin{pmatrix} -\cos 2\vartheta_m & \sin 2\vartheta_m \\ \sin 2\vartheta_m & +\cos 2\vartheta_m \end{pmatrix} \quad (0.22)$$

which leads to the functional dependence as in two-flavor oscillation case of the oscillation probability. By equating Eq. (0.20) and Eq. (0.22), we can derive the expression for the effective mixing parameters in matter

$$\sin^2 2\vartheta_m = \frac{\sin^2 2\vartheta}{\sin^2 2\vartheta + (\cos 2\vartheta - \xi)^2} \quad (0.23)$$

and

$$\Delta m_{eff}^2 = \Delta m^2 \cdot \sqrt{\sin^2 2\vartheta + (\cos 2\vartheta - \xi)^2}. \quad (0.24)$$

In matter the neutrino and anti-neutrino mixings are different because ν and $\bar{\nu}$ have opposite effective potentials. The eigenvalue/eigenvector solutions for anti-neutrinos can be obtained with the replacement $V \rightarrow -V$ or $\xi \rightarrow -\xi$.

It is easy to verify that the limit $\xi \rightarrow 0$ recovers the vacuum case. The limits $\xi \rightarrow \pm\infty$ correspond to very large density for neutrinos or antineutrinos. The effective

mixing parameters become

$$\sin^2 2\vartheta_m \rightarrow \frac{\sin^2 2\vartheta}{\xi^2} \rightarrow 0 \quad ; \quad \Delta m_{eff}^2 = \Delta m^2 \cdot \xi = \pm 2EV . \quad (0.25)$$

It can be seen that Eq. (0.23) corresponds to $\vartheta_m \rightarrow \pi/2$ (for ν_e). In other words, when the potential difference V becomes much larger than the energy differences $\Delta m^2/2E$, the weak-interaction eigenstates become eigenstates of propagation: $|\nu_e\rangle$ (with $V > 0$) corresponds to the heaviest eigenvector $|\nu_2\rangle$ ².

Another important situation occurs under the resonant condition $\cos 2\vartheta - \xi = 0$ in (0.23). In this case, oscillations can be significantly enhanced, irrespectively of the value of ϑ , therefore even if the vacuum oscillation probability is very small. The energy for which the resonant condition occurs is given by (using $\vartheta = \theta_{12}$ and $\Delta m^2 = \Delta m_{12}^2$):

$$E_{res} = \frac{\Delta m_{12}^2 \cos 2\theta_{12}}{2\sqrt{2}N_e G_F} \quad (0.26)$$

and it is referred to as the *resonance energy*. Correspondingly, the electron density $N_{e,res}$ for which at a given energy E there is a resonant condition is called *resonance density*.

In the Sun, the electron number density N_e changes considerably along the neutrino path. In the core, the matter density is about $\rho \sim 150 \text{ g/cm}^3$ and it decreases monotonically to 0 at the surface. Using the best-fit values obtained by KamLAND

$$\Delta m_{12}^2 = (7.9 \pm 0.6) \cdot 10^{-5} \text{ eV}^2 \quad ; \quad \tan^2 \theta_{12} = (0.40 \pm 0.10) , \quad (0.27)$$

in (0.26) with the density of the Sun core in (0.19), we obtain the minimum energy for which the resonance condition occurs, which is of the order of $E_{res}^{min} \sim 1 \text{ MeV}$.

It is not difficult to understand qualitatively the possible behavior of ν_e from the center to the surface of the Sun if one realizes that one is dealing effectively with a two-levels system whose Hamiltonian depends on time and admits jumps from one level to the other. Below $\sim 1 \text{ MeV}$, $E/\Delta m^2$ is sufficiently small so that a resonant density condition is never fulfilled and $\xi \rightarrow 0$ in (0.20), the oscillations take place in the Sun as in vacuum and

$$P(\nu_e \rightarrow \nu_e) \simeq c_{13}^4 P + s_{13}^4 \quad (0.28)$$

with

$$P = 1 - \sin^2 2\theta_{12} \sin^2 \left(\frac{\Delta m_{12}^2}{4E} L \right) \quad (0.29)$$

holds. Using the Sun-Earth distance $L = D_\odot$ then $E/L \gg \Delta m_{12}^2$ and as usual the average value of the $\sin^2 x$ function must be used. Thus, the electron neutrino survival probability becomes

² Although not relevant for solar neutrinos, it is interesting to note that the $|\bar{\nu}_e\rangle$ (with $V < 0$) corresponds to the lightest eigenvector $|\nu_1\rangle$. Matter interactions has a different effect on neutrinos and antineutrinos.

$$P_{ee} \equiv P(\nu_e \rightarrow \nu_e) = 1 - \frac{\sin^2 2\theta_{12}}{2} \quad E < 1 \text{ MeV} \quad (0.30)$$

exactly as for atmospheric ν_μ oscillations

$$P(\nu_\mu \rightarrow \nu_\mu) = 1 - \frac{\sin^2 2\vartheta}{2} \text{ for } E/L \gg \Delta m^2 \quad (0.31)$$

with the appropriate mixing angle. This expression describes with good precision the transitions of the lower-energy solar neutrinos, those of the pp reaction with $E < 0.42$ MeV. On the opposite side, the high energy limit corresponds to the ${}^8\text{B}$ transitions with $E \gtrsim 5$ MeV observed by SK and SNO experiments. The probability can be expressed as

$$P_{ee}({}^8\text{B}) \simeq \sin^4 \theta_{13} + \cos^4 \theta_{13} \sin^2 \theta_{12} \quad E \gg 1 \text{ MeV} \quad (0.32)$$

The data show that $P_{ee}({}^8\text{B}) \simeq 0.3$, which is a strong evidence for matter effects in the solar ν_e transitions. Note that in both the vacuum- and matter-dominated oscillation regimes, the ν_e survival probability depends only on the mixing angles; neither the neutrino mass splitting nor the details of the neutrino-matter interactions appear. Instead, these factors determine the position and shape of the transition between the two regimes ($\xi \rightarrow 0$ or $\xi \rightarrow +\infty$) and the passage through the resonance region, which occurs between neutrino energies of approximately 1 and 3 MeV. As the neutrino energy increases, the ν_e propagation can be studied numerically.

Extra 7: Experimental limits on Grand Unification Theories

In the Standard Model structure, quarks and leptons are placed in separate multiplets. In the first family, there are two quarks [the (u, d)] and two leptons [(ν_e, e)]. Baryon number conservation forbids the proton decay. However, there is no known gauge symmetry which generates baryon number conservation. Therefore, the validity of baryon number conservation must be considered as an experimental question.

Grand Unified Theories place quarks and leptons in the same multiplets; we may think that quarks and leptons are, at the low energies of our laboratories, different manifestations of a single particle. At very high energies, therefore, quark \leftrightarrow lepton transitions are possible: they are mediated by massive X, Y bosons, respectively with electric charges of $4/3$ and $1/3$. Because the mass of these gauge bosons are predicted to be very large, such processes are expected to be very rare. Below 10^{15} GeV, the unification among forces foreseen by GUTs ceases through a spontaneous symmetry breaking, giving rise to the symmetries of the Standard Model.

Proton Decay

Starting from the 1980s, the search for proton decay was the main reason for developing large detectors and underground laboratories [E-02]. The simplest GUT model, called SU(5), predicts a proton lifetime value of $\tau_p \sim 10^{30}$ years. The expected number of decay events per year is

$$N = \frac{f \cdot N_N \cdot M_F \cdot T \cdot \varepsilon}{\tau_p} \quad (0.33)$$

where $f = p/(p+n)$ is the proton fraction in the target, N_N is the number of nucleons in 1 kt mass ($\sim 6 \cdot 10^{23} \cdot 10^9$), M_F (in kt) is the fiducial mass, T is the detector lifetime (in years) and ε is the overall detection efficiency. You can verify immediately that the simplest GUT prediction leads to the possible observation of many proton decay events in a kt-scale detector.

For nucleon decay searches, the most competitive experimental techniques use water Cherenkov detectors and tracking calorimeters, already introduced in §11.7. The main proton decay channels predicted from SU(5) are $p \rightarrow e^+ \pi^0$ and $\mu^+ \pi^0$. The proton at rest decays in two light particles, carrying the 938 MeV of its rest mass. These processes are almost free from backgrounds different from that induced by atmospheric neutrinos in the GeV energy range. A large fraction of this background can be suppressed by selecting events well contained in the detector fiducial volume and by applying topological and kinematical constraints.

The largest experiment currently taking data is Super-Kamiokande (SK), §11.9, with a total mass of ~ 50 kt and an inner *fiducial volume* of 22.5 kt.

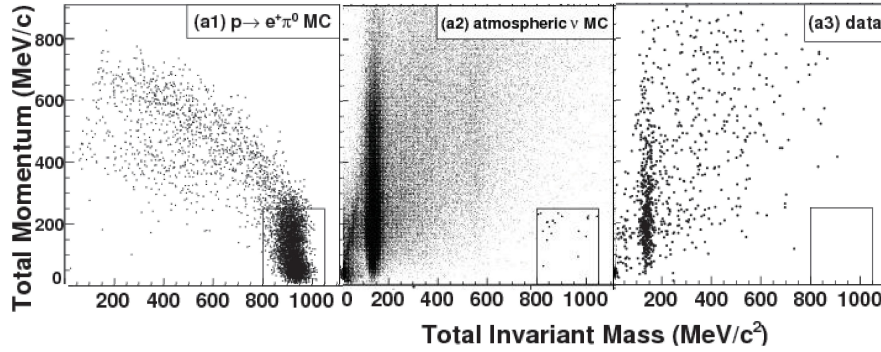


Fig. 0.8 Total momentum versus total invariant mass distributions for Monte Carlo (MC) proton decay events (left panel), 500 year-equivalent MC atmospheric neutrino events (central panel) and data (right panel). The boxes in the plots indicate the region in which the signal is expected. Points in the signal box of the atmospheric neutrino MC are shown with a larger size. Credit: Kamioka Observatory, ICRR (Institute for Cosmic Ray Research), The University of Tokyo

In SK, the e^+ (or μ^+) produces Cherenkov light. The photons arising from the π^0 decay, $\pi^0 \rightarrow \gamma\gamma$, originate an electromagnetic shower which produces a signal similar to that of the electron, see Fig. 11.11a). The intersection of the Cherenkov light cone with the instrumented detector surface generates signals having the shape of “rings”. In multi-ring events, as expected for hypothetical proton decays, the directions and opening angles of visible Cherenkov rings are reconstructed, and each identified ring is classified as a showering electron-like ring or a non-showering muon-like ring (Fig. 11.11b). The particle momentum is estimated by the number of detected photoelectrons. To search for a proton decay signal, only events with two or three rings have been selected. In $p \rightarrow e^+ \pi^0$ events, all the rings should be e -like. One non-showering ring (μ -like) is required for $p \rightarrow \mu^+ \pi^0$ candidates.

Proton decays (signal) and atmospheric neutrino interactions (background) have been simulated using Monte Carlo procedures, taking into account accurate simulation of the detector response. For each simulated signal and background event, the reconstructed total momentum and total energy are inserted in a two-dimensional

plot (first two panels of Fig. 0.8). From the null signal (no real data are present in the box signal of the third panel of Fig. 0.8), using Eq. (0.33), SK was able to derive the strongest limits on the proton lifetime: $\tau_p > 8.2 \times 10^{33}$ and 6.6×10^{33} years at the 90% C.L. for $p \rightarrow e^+ \pi^0$ and $p \rightarrow \mu^+ \pi^0$, respectively [E-06]. These experimental limits exclude the simplest GUT models (which predicts a proton decay lifetime smaller than the experimental lower limits). Many more proton decay modes have been searched for, all with null results. At present, larger project are proposed to improve by more than one order of magnitude the limit on the proton lifetime.

Despite its beauty, the simplest GUT model based on SU(5) should be rejected. There are indeed other models based on more complex groups, for example SO(10), that have more parameters and provide longer lifetimes. The combination of the supersymmetry with GUT allows one to consider the $p \rightarrow K^+ \nu$ decay as the most probable. This leads to a longer proton lifetime, about 10^{33} year; the current experimental limit (see the Baryon Summary Table of [E-08]) is $\tau_p > 2.3 \cdot 10^{33}$ year.

Magnetic Monopoles

GUT theories require the existence of supermassive *magnetic monopoles* (MMs), [E-01]. They could be created as point-like topological defects at the time of the Grand Unification symmetry breaking into subgroups at 10^{15} GeV. These MM should have a mass m_M equal to the mass of the massive X, Y bosons, divided by the unified coupling constant α at 10^{15} GeV, $m_M \simeq m_X/\alpha \sim 10^{15}/0.03 \sim 3 \times 10^{16}$ GeV/c². The MM magnetic charge g is predicted by the Dirac relation, $eg = n\hbar c$, where n is an integer. If we take as the elementary electric charge that of the electron and $n = 1$, we have $g = 68.5e$ in the symmetric unit system of Gauss. The value of the magnetic charge g is therefore huge. The introduction of MMs in the Maxwell equations produce a complete symmetry between electric and magnetic fields; the symmetry is “numerically broken” by the value of magnetic charge, much larger than the electric one, and by the incredibly large mass of MMs, $m_M \sim 10^{16}$ GeV/c².

The velocity range in which relic GUT magnetic monopoles should be sought spreads over several decades. GUT magnetic monopoles would be gravitationally bound to the Galaxy (Solar System) with a velocity distribution peaked at $\beta = v/c \sim 10^{-3}$ (10^{-4}). Lighter magnetic monopoles with masses around $10^7 \div 10^{15}$ GeV/c², eventually produced in later phase transitions in the early Universe, would be accelerated to relativistic velocities in one or more coherent domains of the galactic magnetic field, or in the intergalactic field, or in proximity of several astrophysical sites like a neutron star.

Theory does not provide definite predictions on the magnetic monopole abundance. However, by requiring that MMs do not short-circuit the galactic magnetic field faster than the dynamo mechanism can regenerate it, a flux upper limit can be obtained. This is the so-called Parker bound ($\Phi_{MM} \lesssim 10^{-15} \text{ cm}^{-2} \text{ s}^{-1} \text{ sr}^{-1}$), whose value sets the scale of the detector exposure for MM searches.

The largest apparatus constructed to detect GUTs MM was the MACRO experiment (§11.9.3), with a total acceptance to an isotropic flux of particles of $\sim 10^8 \text{ cm}^2 \text{ sr}$. It used three different experimental techniques able to catch the MM signature: scintillator counters, limited streamer tubes and nuclear track detectors. The details about how these sub-detectors are sensible to the passage of a magnetic charge and on the experimental techniques can be found in [E-04]. No MM candidate was found in the velocity range $4 \times 10^{-5} < \beta < 1$ and the 90% C.L. upper limit to the local magnetic monopole flux was set at the level of $1.4 \times 10^{-16} \text{ cm}^{-2} \text{ s}^{-1} \text{ sr}^{-1}$. This limit is below the Parker bound in the whole β range in which GUT magnetic monopoles are expected. The MACRO limit also excludes MMs as a significant component of the *dark matter* in the Universe.

References

- E-01. G. Giacomelli. *Magnetic monopoles*. La Rivista del Nuovo Cimento 7, N. 12 (1984) 1.
- E-02. D.H. Perkins. *Proton Decay Experiments*. Annual Review of Nuclear and Particle Science 34 (1984) 1-50.
- E-03. P. Lipari and T. Stanev. *Propagation of multi-TeV muons*. Phys. Rev. D44 (1991) 3543, doi: 10.1103/PhysRevD.44.3543.
- E-04. M. Ambrosio et al. *Final results of magnetic monopole searches with the MACRO experiment*. Eur. Phys. J. C 25 (2002) 511-522.
- E-05. D.N. Spergel et al. (WMAP Coll.). *Wilkinson Microwave Anisotropy Probe (WMAP) three year results: implications for cosmology*. Astrophys. J. Suppl. 170 (2007) 377. Also: astro-ph/0603449.
- E-06. H. Nishino et al. (Super-K Collaboration). *Search for Proton Decay via $p \rightarrow e^+ \pi^0$ and $p \rightarrow \mu^+ \pi^0$ in a Large Water Cherenkov Detector*. Physical Review Letters 102 (2009) 141801.
- E-07. S. Braibant, G. Giacomelli, M. Spurio. *Particle and fundamental interactions*. Springer (2011). ISBN 978-9400724631.
- E-08. J. Beringer et al. (Particle Data Group). *The Review of Particle Physics*. Phys. Rev. D86 (2012) 010001. See <http://pdg.lbl.gov/>
- E-09. S. Braibant, G. Giacomelli, M. Spurio. *Particles and Fundamental Interactions: Supplements, Problems and Solutions*. Springer (2012). ISBN 978-9400741355
- E-10. Planck Release 2013 Papers. ArXiv: from 1303.50965 to 1303.5090

